Gold Au(I)$_6$ Clusters with Ligand-Derived Atomic Steric Locking: Multifunctional Optoelectrical Properties and Quantum Coherence

Sourov Chandra,* Alice Sciortino, Susobhan Das, Faisal Ahmed, Arijit Jana, Jayoti Roy, Diao Li, Ville Liljeström, Hua Jiang, Leena-Sisko Johansson, Xi Chen,* Nonappa, Marco Cannas, Thalappil Pradeep, Bo Peng, Robin H. A. Ras, Zhipei Sun, Olli Ikkala,* and Fabrizio Messina*

An atomically precise ultrasmall Au(I)$_6$ nanocluster where the six gold atoms are complexed by three sterically interlocking stabilizing ligands is reported, allowing a unique combination of efficient third harmonic generation (THG), intense photoluminescence quantum yield (35%), ultrafast quantum coherence, and electron accepting properties. The reaction of 6-(dibutylamino)-1,3,5-triazine-2,4-dithiol (TRZ) with HAuCl$_4$ leads to complexation by thiolation. However, intriguingly, another reduction step is needed to form the centrosymmetric Au(I)$_6$TRZ$_3$ clusters with the multifunctional properties. Here, ascorbic acid is employed as a mild reducing agent, in contrast to the classic reducing agents, like NaBH$_4$ and NaBH$_3$CN, which often produce mixtures of clusters or gold nanoparticles. Such Au(I)$_6$ nanocluster films produce very strong THG response, never observed for nanoclusters. The clusters also produce brilliant single and multiphoton luminescence with exceptional stability. Density functional theory calculations and femtosecond transient absorption studies suggest ultrafast ligand-to-metal charge transfer, quantum coherence with long decoherence time 200–300 fs, and fast propagation of excitation from the core to the surrounding solvent. Finally, novel electron-accepting ground state properties allow *p*-doping of 2D field-effect transistor devices. Summarizing, the potential of ultrasmall sterically interlocked Au(I) clusters, i.e., complexes allowed by the new sequential reduction protocol, towards multifunctional devices, fast photoswitches, and quantum colloidal devices is shown.

1. Introduction

Gold nanoclusters and small gold complexes have attracted considerable attention due to their fundamental properties and application potential upon bridging the functional gap between molecules and larger plasmonic nanoparticles.[1] Atomically precise ultrasmall gold nanoclusters (GNCs) typically have contained an exact number of ≈10 – 300 gold atoms aiming at well-defined particle sizes. They are stabilized by protecting ligands, whereupon their binding typically leads to outer metal surfaces with different valence than that of the inner metal core.[2] Their photo-physics is more complex than that of small molecules and larger quantum dots, leading to both challenges and suggesting novel application possibilities. GNCs allow several relevant properties, such as luminescence with promoted photostability combining biocompatibility.[3–7] Unlike larger plasmonic nanoparticles, GNCs display molecule-like electronic spectra, as their electronic structure is

S. Chandra, X. Chen, B. Peng, R. H. A. Ras, O. Ikkala
Department of Applied Physics
Aalto University
P. O. Box 15100, Espoo, Aalto FI-00076, Finland
E-mail: sourov.chandra@aalto.fi; xi.6.chen@aalto.fi; olli.ikkala@aalto.fi

A. Sciortino, M. Cannas, F. Messina
Dipartimento di Fisica e Chimica – Emilio Segrè
Università degli Studi di Palermo
Via Archirafi 36, Palermo 90123, Italy
E-mail: fabrizio.messina@unipa.it

A. Sciortino, F. Messina
CHAB – ATeN Center
Università degli studi di Palermo
Viale delle Scienze, Edificio 18, Palermo 90128, Italy

S. Das, F. Ahmed, D. Li, Z. Sun
Department of Electronics and Nanoengineering
Aalto University
Maarintie 13, Espoo 02150, Finland

A. Jana, J. Roy, T. Pradeep
Department of Chemistry
DST Unit of Nanoscience (DST UNS) and Thematic Unit of Excellence (TUE)
Indian Institute of Technology Madras
Chennai 600036, India

V. Liljeström, H. Jiang
Nanomicroscopy Center
OtaNano
Aalto University
Aalto FI-00076, Finland

L.-S. Johansson
Department of Bioproducts and Biosystems
Aalto University
Vuorimiehentie 1, Espoo FI-00076, Finland

dominated by delocalized states spread over a relatively large Au core. Beyond that, there is a scientific interest toward in-depth understanding of GNC photocycle.[8–17] In particular, studies using relatively large Au_{13} and Au_{25} clusters, often modeled within the "superatom" theoretical framework, suggest that the optically active electronic states are localized within the gold cores.[8,16–19] Recent theoretical calculations suggest that all excited states may arise from core-based superatomic orbitals.[16] Importantly, the protecting ligands also play a role in the electronic response of the GNCs through ligand-to-metal charge transfer (LMCT) transitions[10,14,15] or by so-called semi-ring states.[11] Still, recently questions have been posed whether the knowledge accumulated on classical GNCs such as Au_{25}, containing both Au(0) and Au(I) atoms, can directly apply to ultrasmall GNCs containing less than ten Au atoms where all atoms are in Au(I) state due to the ligand binding, also related to new properties. Such GNC structures have recently also been specifically denoted as Au(I) complexes.[1]

Regarding to optical applications, a materials platform allowing tunably multifunctionality would be highly desired. For optical nonlinearities, the basis for all-optical devices employs self-phase modulation, optical bistability, regenerative oscillations, and four-wave mixing.[20] Due to their applications in imaging, medicine, communication, and industry, the present demand for devices motivates the assessment of the nonlinear optical (NLO) properties of materials in visible and near-infrared region.[21,22] Traditional bulk NLO materials, such as β-BaB_2O_4 and $LiNbO_3$, suffer from low conversion efficiency and poor NLO susceptibility.[23] Two-dimensional (2D) nanomaterials such as graphene, hexagonal boron nitride, transition-metal dichalcogenides, and GeAs show strong second and third-harmonic generation (SHG and THG) stemming from their crystal noncentrosymmetry.[21,24–26] However, they do not display combined strong photoluminescence (PL), robust harmonic generation, or electric doping, thus they have not shown multifunctionality so far.

Therefore, one can foresee a need to develop materials having both advanced linear and nonlinear optical properties with high conversion efficiency and high nonlinear susceptibility, as well as electric functionality. Therein, developing biocompatible molecular level clusters below 1 nm would offer potential applications not only in devices but also in medicine as such particles can readily cross the blood-brain barrier.[27,28] Gold nanoparticles have been investigated for NLO properties.[29] THG has been reported for isolated gold nanorods and nanoparticles of specific shapes and sizes using highly sophisticated designs for plasmonic nanoparticles.[29] Nevertheless, plasmonic nanoparticles typically involve polydispersity, therefore, achieving THG is a fundamental challenge. Recent experimental and theoretical studies have shown that gold and

silver nanoclusters also exhibit SHG.[30] However, multifunctional ultrasmall GNCs displaying THG have not been reported, even more to combine with luminescence. Also, showing GNC-dependent doping of semiconductor devices could allow new modular approaches, not shown before.

Herein, we report the synthesis and optoelectronic properties of 6-(dibutylamino)-1,3,5-triazine-2,4-dithiol (TRZ) stabilized GNCs containing a metal core of six gold atoms $Au(I)_6$, i.e., where all gold atoms are in the Au(I) state and the vibration of the atoms is locked by the TRZ ligands via dual thiolate bindings. This is done by a novel two-step chemical reduction. The experimental data along with density functional theory (DFT) calculations suggest that the $Au(I)_6$ core has an octahedral geometry, resulting in a triclinic crystal lattice in solid state. The centrosymmetric Au-core produces an intense THG under infrared laser excitations. The particles exhibit a strong third-order susceptibility. They also display strong PL with high quantum efficiency and peculiar photophysical behavior unlike larger nanoclusters. The photocycle is controlled by ligand-to-metal charge transfer transitions without intermediates. Moreover, we show that the energy cascade from the initially excited state proceeds through a coherent pathway, involving the generation of core vibrational wave packets damped through successive relaxation. As a result, GNCs induce a controllable *p*-type (hole dominant) doping effect to the 2D multilayer WSe_2 field effect transistors (FETs) through a charge transfer mechanism.

2. Results and Discussion

2.1. Synthesis and Characterizations

The reaction of 6-(dibutylamino)-1,3,5-triazine-2,4-dithiol (TRZ) with $HAuCl_4$ leads to complexation and gold reduction by thiolation, but results in uncontrolled fibrillar aggregates (Figure S1, Supporting Information). To achieve spherical well-controlled nanoclusters of TRZ-stabilized GNCs, another reduction step by preferably ascorbic acid (denoted as GNC-1) or alternatively by $NaBH_4$ (denoted as GNC-2) was required (**Figure 1**a). The scanning transmission electron microscopy (STEM) images of GNC-1 and GNC-2 are presented in Figure 1b,c respectively, suggesting uniform distribution of clusters with a size of ~1 nm. The resulting GNCs exhibit intense yellow-green emission under exposure to UV light (inset in Figure 1b). The energy-dispersive X-ray (Figure S2, Supporting Information) and the X-ray photoelectron spectra (XPS) (Figure S3, Supporting Information) confirm the elements Au, S, C, O, and N. While C 1s, N 1s, and S 2p spectra further approve the C–C, C–H, C–N, –C≐N–C, ≐N–C≐ , and Au–S bonds (Figure S4, Supporting Information), the Au 4f doublet at 85.0 and 88.7 eV confirms the existence of Au(I) atoms in both GNC-1 and GNC-2 (Figure 1d). Finally, electrospray ionization mass spectra (ESI-MS) in both negative and positive ion modes confirm the composition as $Au(I)_6(TRZ)_3$ (Figure 1e and Figure S5, Supporting Information). The results indicate the coexistence of both -2 and +1 states of the GNCs and that they are in equilibrium. The collision energy-dependent studies show the fragmentation of the clusters (Figure S6, Supporting

Nonappa
Faculty of Engineering and Natural Sciences
Tampere University
Korkeakoulunkatu 6, P. O. Box 541, Tampere FI-33101, Finland

Z. Sun
QTF Centre of Excellence
Department of Applied Physics
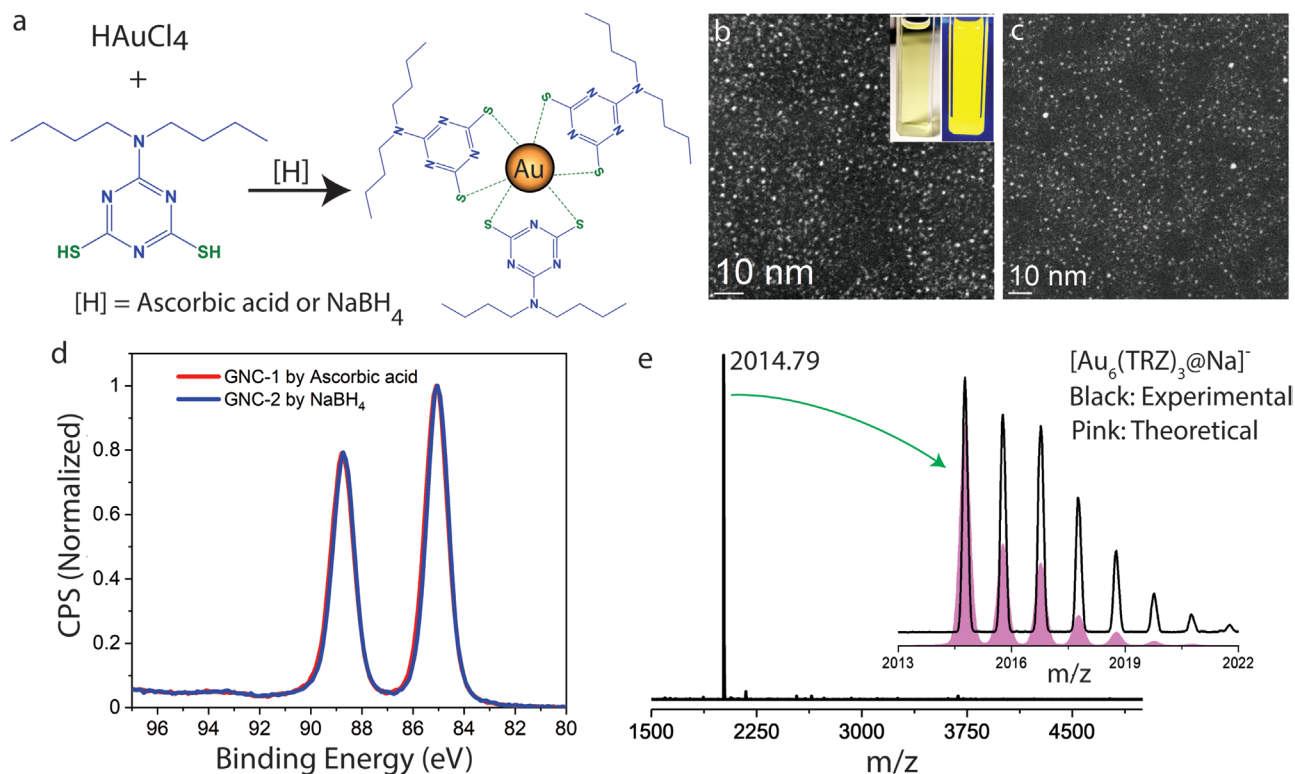Aalto University
Aalto FI-00076, Finland

Figure 1. a) Schematic representation for the synthesis of GNCs. STEM images of b) GNC-1 and c) GNC-2. Inset in (b) shows the dichloromethane (DCM) solution of GNCs under ambient light (left) and exposure to UV light (right). d) Au 4f XPS spectra of GNCs. e) Electrospray ionization mass spectrum of GNC-1, suggesting a composition $Au(I)_6(TRZ)_3$ based on experiment and modeling.

Information). The ^{1}H NMR spectra of the free TRZ-ligand and the GNCs (Figures S7 and S8, Supporting Information) further support their compositions and nature of fast protonation and deprotonation.

2.2. DFT Calculations and Mapping of Electronic Transitions

Based on ESI-MS, the atomic models of $[Au(I)_6(TRZ)_3]^{2-}$ and $[Au(I)_6(TRZ)_3]^+$ GNCs are created using DFT with GPAW code.[31] Two possible isomers of $[Au(I)_6(TRZ)_3]^{2-}$ NCs are produced (**Figure 2**a,b), wherein the latter one shows the most stable structure consisting of an octahedral $Au(I)_6$ core surrounded by three TRZ ligands. The average Au–Au and Au–S bond lengths are 2.84 and 2.38 Å, respectively. The HOMO-LUMO energy gap of the cluster is 1.43 eV; the HOMO states have contributions both from the ligands and Au atoms, while the electrons in the Au atoms dominate the LUMO states (Figure 2c). The time-dependent DFT[32] simulated optical absorption (OA) spectrum from the octahedral $[Au(I)_6(TRZ)_3]^{2-}$ GNC displays two distinct peaks at 413 and 318 nm (Figure 2d). The computed spectral patterns are close to the experimental OA with a slight red shift.[33] To get insight into electron-hole transitions responsible for the absorption ≈400 nm, we analyzed the transitions at 3.0 eV (413 nm) using the transition contribution map (TCM) method.[34] The TCM in Figure 2e demonstrates the Kohn–Sham (KS) absorption decomposition weight at a fixed energy ω in the two-dimensional

$(\varepsilon_o, \varepsilon_u)$- plane, where ε_o and ε_u are the energies of the occupied and unoccupied states, respectively. The corresponding projected density of states (PDOS) are plotted on the top and right side of the TCM, respectively. It implies that the most significant contribution for the OA at 413 nm is due to the electronic transitions from the occupied states at −1.14 eV to the unoccupied states ≈1.78 eV (Fermi level is set to 0 eV). Figure 2f shows the wave functions at −1.14 eV and 1.78 eV, in which the ligands significantly contribute to the occupied states while the Au atoms dominate the unoccupied states, i.e., the OA at ≈400 nm is due to the ligand to metal electron-hole or charge transfer transitions. Regarding $[Au(I)_6(TRZ)_3]^+$, one proton is added to each ligand, which changes the cluster's charge from −2 to +1 (Figure S9, Supporting Information). The calculated OA spectra of deprotonated $[Au(I)_6(TRZ)_3]^{2-}$ and protonated $[Au(I)_6(TRZ)_3]^+$ NCs are quite similar (Figure S10, Supporting Information), indicating the analogous electron-hole transitions in these two systems.

The small angle X-ray diffraction pattern of the GNC-1 and pure ligand are shown in Figure S11a,b, Supporting Information, respectively. The diffraction pattern (Figure 2g) is calculated by including the octahedral gold core of the nanocluster to the best-fitting crystal lattice. Ligand molecules are not included in the model. The theoretical diffraction pattern corresponds to the triclinic crystal structure (space group P1, number 1) with unit cell dimensions a = 11.85 Å, b = 9.81 Å, c = 8.37 Å, and unit cell angles α = 85.7°, β = 85.3°, γ = 98.2° (Figure 2h). The volume of the unit cell is 956.1 Å^3.

ADVANCED
SCIENCE NEWS

www.advancedsciencenews.com
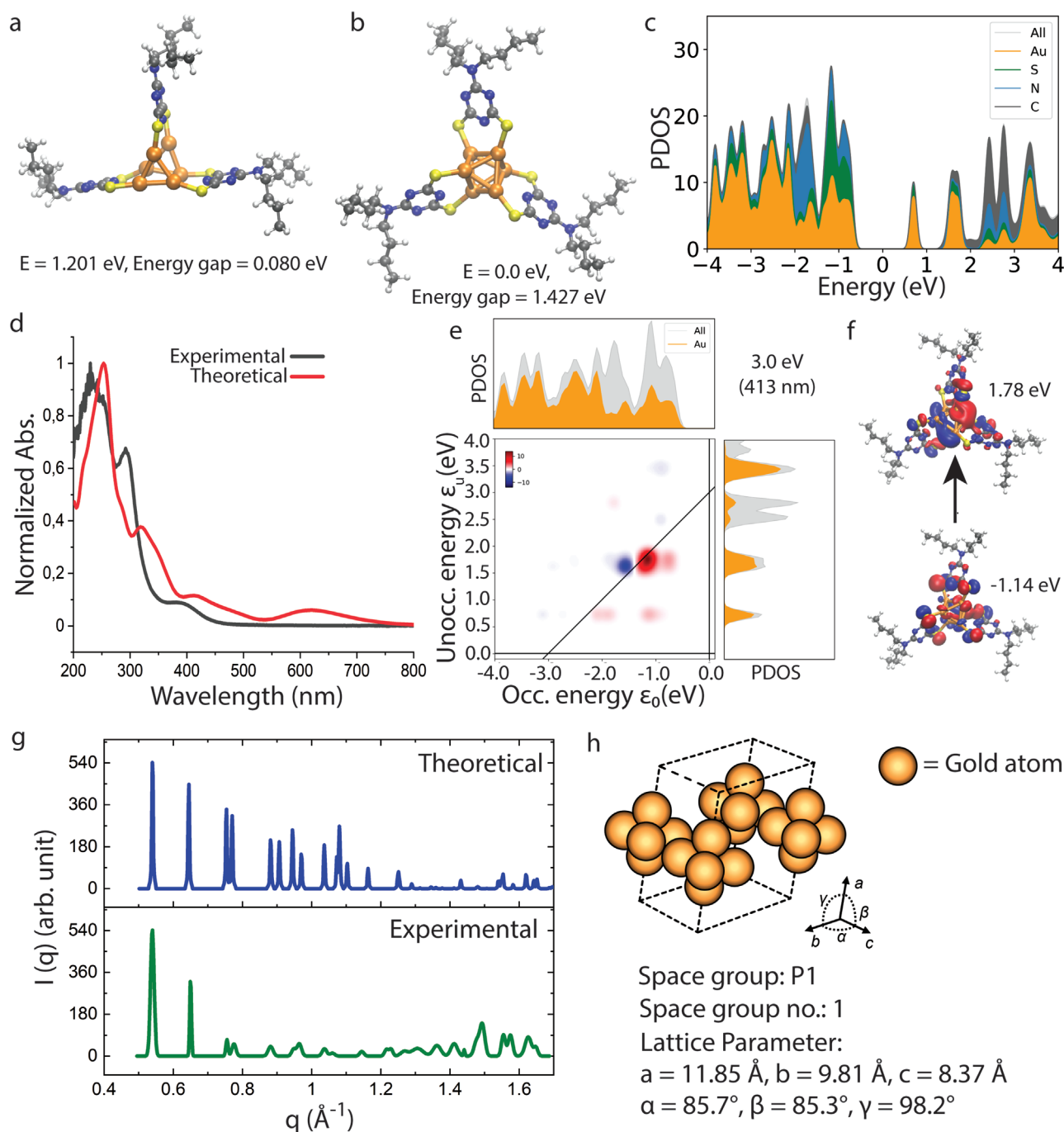
ADVANCED
OPTICAL
MATERIALS

www.advopticalmat.de

Figure 2. a,b) The atomic structures for two different isomers of [Au(I)$_6$(TRZ)$_3$]$^{2-}$ optimized by DFT, where (b) shows the lowest energy structure with octahedral Au(I)$_6$ core. c) The projected density of states of the most stabilized octahedral core of the cluster, shown in (b). d) Experimental and theoretical OA spectra of GNC-1. e) The TCM map and PDOS of the cluster at 3.0 eV (413 nm). f) The highest contribution of OA from the occupied state at −1.14 eV to the unoccupied state at 1.78 eV, assuming the Fermi level at 0 eV. g) Calculated diffraction peaks and the theoretical diffractogram based on the triclinic crystal structure. h) The unit cell of the proposed triclinic crystal structure (ligands are excluded in the model).

2.3. Linear and Nonlinear Optical Responses

The photoluminescence (PL) spectra of GNC-1 and GNC-2 are quite similar, with broad emissions centered at ≈540 nm (**Figure** 3a). The photoluminescence excitation (PLE) spectrum

of the 540 nm emission displays two peaks at 327 and 400 nm for both GNCs. When exciting in the LMCT state at 400 nm, the emission peak at 540 nm with absolute quantum yield of ≈35% and decay over a few microseconds (Figure 3b) are observed, almost identically in GNC-1 and GNC-2 (Figure S12
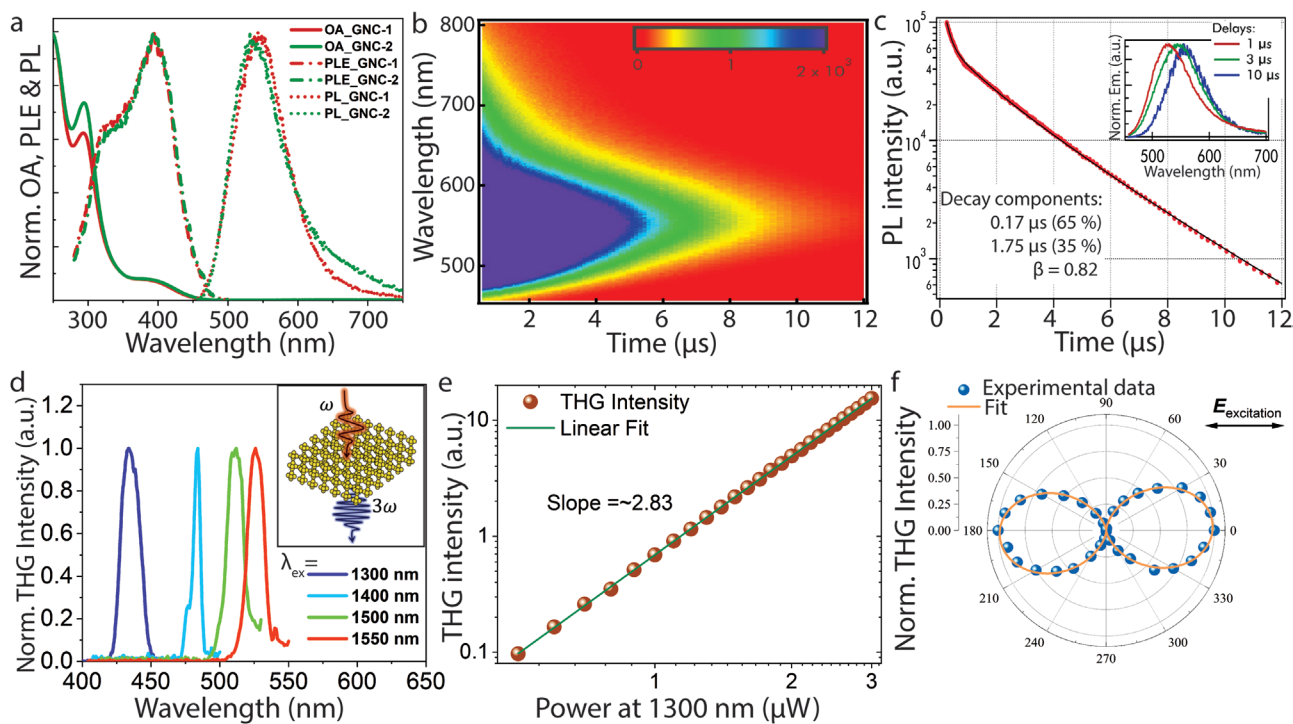
2202649 (4 of 8)

**ADVANCED
SCIENCE NEWS**

www.advancedsciencenews.com

**ADVANCED
OPTICAL
MATERIALS**

www.advopticalmat.de

Figure 3. a) Optical absorption (OA), steady-state PL (λ_{ex} = 400 nm), and PLE (λ_{em} = 540 nm) spectra of GNC-1 and GNC-2 in DCM. b) Time-resolved PL spectra of GNC-1 at 410 nm excitation. c) Decay kinetics of the spectrally integrated PL signal. The data are fitted by a biexponential decay function, that is: $I = A \exp[-t/t_1] + B \exp[-(t/t_2)^b]$. The stretching factor b in the slower exponential is a typical feature of disordered systems, consistent with the progressive shift of the emission during decay shown in its inset. Inset: Normalized PL spectra at various delays after photoexcitation. d) THG emissions from the thin film of GNC-1 at 1300, 1400, 1500, and 1550 nm excitations. Inset: Schematic diagram of THG process in Au(I)$_6$ NCs. The top and bottom waves indicate the excitation beam (ω) and the generated THG signal (3ω), respectively. e) Excitation power dependency of THG signal of the GNC film at 1300 nm excitation. f) THG response as a function of excitation polarization.

Supporting Information). The emission decay is bi-exponential (0.17 µs + 1.75 µs) (Figure 3c), revealing two quasi-degenerate emitting states, most likely due to the coexistence of two different charge states of the NC: [Au(I)$_6$(TRZ)$_3$]$^+$ and [Au(I)$_6$(TRZ)$_3$]$^{2-}$. Besides, an appreciable redshift of the band during decay (inset of Figure 3c) suggests a further statistical distribution of lifetimes. The observed microsecond lifetimes imply a weakly allowed emissive transition. The PL is strongly Stokes shifted (>150 nm) and lacks mirror symmetry from the lowest-energy absorption band. Therefore, the emissive state is presumably characterized by a significant triplet character, i.e., the emission stems from a ^{3}LMCT state populated indirectly from the ^{1}LMCT state excited at 400 nm through an intersystem crossing process (ISC) (Figure S13, Supporting Information).

Interestingly, the GNCs show a strong nonlinear optical effect, particularly for THG (depicted in Figure 3d). The lack of even-order harmonics along with such intense THG can be explained by an inversion symmetry in the molecular structure of these octahedral [Au(I)$_6$(TRZ)$_3$]$^{2-}$ nanoclusters. When illuminated by ultrafast infrared lasers at variable wavelengths, GNC-1 produces strong THG signals at ≈433, 470, 500, and 520 nm, corresponding to frequency tripling by the excitation beams at 1300, 1400, 1500, and 1550 nm, respectively. In addition to the narrow THG peaks, we also observe a broadband signal between 520 to 700 nm, indicating PL caused by three-photon absorption (Figure S14, Supporting Information). The emission band shape is identical when produced by single-,

two-, or three-photon absorption. The power-dependent THG measurements under 1300 nm excitation (Figure 3e) demonstrate that the THG signal intensity ($I_{3\omega}$) is large and increases with incident intensity (I_ω) as $I_{3\omega} = (I_\omega)^\alpha$ with α = 2.83, close to the value of 3 expected for a nonlinear THG process. The polarization of the generated THG is highly dependent on the incident polarization (Figure 3f). With the horizontal polarization of excitation, the THG signal intensity is maximum along the direction of the excitation and minimum at the cross-polarization. The mathematical fit shows a sinusoidal behavior of the generated THG signal with the polarization angle of the detection polarizer. The third-order nonlinear susceptibility is calculated with the formula given as:

$$\chi^{(3)} = \frac{4\varepsilon_0 c^2}{3\omega d} \sqrt{n_\omega^3 n_{3\omega} \frac{I_{3\omega}}{I_\omega^3}} \tag{1}$$

where ε_0, c, and d are the permittivity of vacuum, speed of light in vacuum, and sample thickness respectively. n_ω ($n_{3\omega}$) and I_ω ($I_{3\omega}$) are the refractive index at frequency ω (3ω) and pump (THG) intensity respectively.[35] Based on this, we obtain the third-order susceptibility of GNCs, $\chi^{(3)}$ = 9.73 × 10^{-19} m^2 V^{-2} (see details in Supporting Information).

Femtosecond transient absorption (TA) measurements indicate energy cascade initiated by 400 nm absorption (**Figure 4**a and Figure S15, Supporting Information). Immediately after photoexcitation, the TA signal displays a negative sign, being
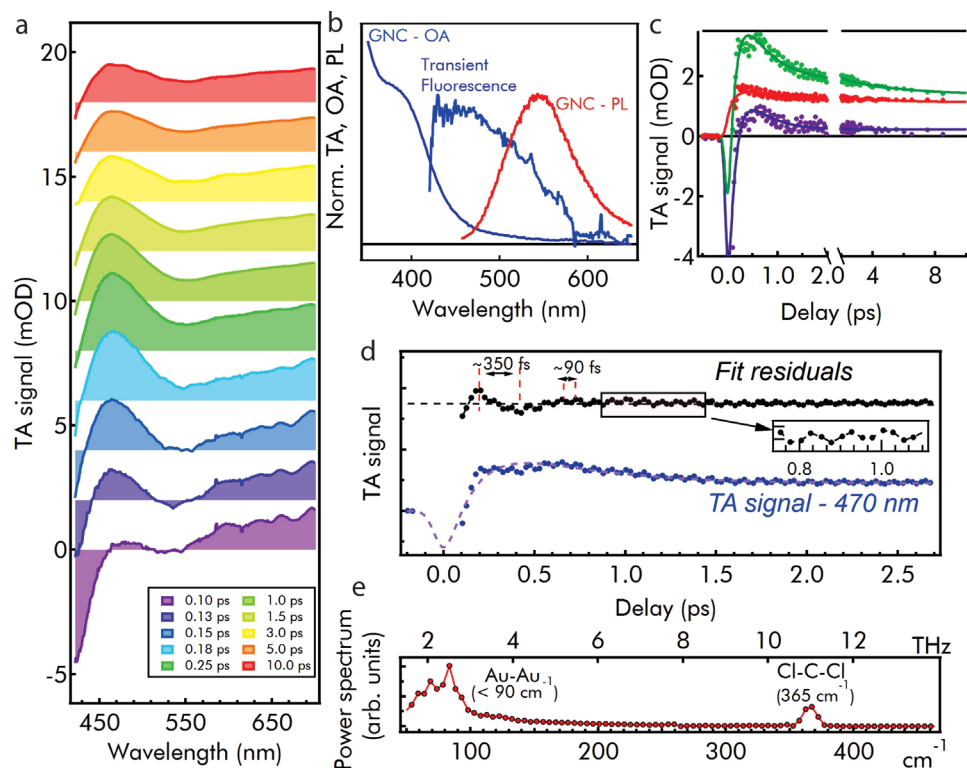
Figure 4. a) Pump-probe transient absorption (TA) spectra recorded at variable delays from femtosecond excitation at 400 nm. b) Transient fluorescence from the electronic state initially excited at 400 nm, isolated as the difference TA (0.18 ps) – TA (0.13 ps), and compared to steady-state OA and PL. c) Kinetic traces of the TA signal, fitted with a three-exponential function convoluted with the Gaussian instrumental response of the TA instrument. d) TA signal at 470 nm (blue dots), fitted by a multi-exponential function describing ISC and further relaxations. The fit residuals (black dots, vertically shifted for the sake of clarity) show coherent oscillations at two different frequencies. e) Fourier transform of the fit residuals at 470 nm.

dominated by ground-state bleaching from the initially excited ^{1}LMCT state and fluorescence, detected in TA as stimulated emission.[36,37] The disappearance of these negative components within ca. 300 fs provides the direct signature of the depopulation of ^{1}LMCT state via ISC, in favor of the ^{3}LMCT. The extremely short-lived ^{1}LMCT fluorescence can be isolated by taking the difference between two TA spectra at successive times. Indeed, this difference signal is a broad band at ≈450 nm, approximately mirror symmetric to the OA at 400 nm (Figure 4b). The TA signal observed at $t > 0.25$ ps, i.e., after the ultrafast singlet-to-triplet cascade, appears as a broad positive TA signal with a peak at 470 nm, providing a spectral fingerprint of the ^{3}LMCT manifold. The multi-exponential fit of the kinetic traces reveals that these dynamics are described by 0.15 ps, 0.45 ps, and 3.9 ps timescales (Figure 4c). While the fastest one is the time scale of ISC, the longer scales represent relaxation and thermalization within the emissive ^{3}LMCT manifold. Similar trends are observed by TA measurements on GNC-2 (Figure S16, Supporting Information).

Closer analysis of TA data reveals a role of quantum coherent effects in the photocycle, visible as a regular modulation of the TA signal persisting for several ps (Figure 4d). In general, these oscillations in TA are due to the motion of coherent vibrational or excitonic wave packets initiated by ultrashort pulses. The Fourier transform of the residuals calculated from a multi-exponential fit (Figure 4e) pinpoints two main frequencies of ≈90 and 365 cm^{-1}. The latter can be attributed to the Cl–C–Cl

deformation mode of dichloromethane (DCM) in which GNCs are dispersed, while the vibration at 90 cm^{-1} is in the expected range for Au–Au oscillations of the GNC core.[9,14] Thereby, we infer that Au core is impulsively brought out of equilibrium by the additional electron projected inside it by ^{1}LMCT photoexcitation, triggering the onset of Au-Au oscillations. Thereafter, as clearly seen in Figure 4d, this oscillation is damped within 200–300 fs, because the excess vibrational energy is redistributed over the entire GNCs, and finally to the solvent, during the ISC process. Further details can be obtained by time-frequency analysis of the fit residuals (Figure S17, Supporting Information). This analysis confirms an instantaneous activation of the Au–Au oscillation, the damping of which is accompanied by the growth of solvent oscillations. Most importantly, the Cl–C–Cl oscillation (365 cm^{-1}) appears progressively growing in amplitude and upshifting in frequency until it is fully established after a delay of ≈300 fs, that is about twice the time scale of ISC. Such a delayed activation of solvent oscillations reports the arrival of the perturbation to the nearest solvent molecules in contact with the ligands, reaching as far as ≈1 nm from the Au core within an extremely short (200-300 fs) time scale. Indeed, we conclude that the whole relaxation cascade of this ultrasmall NC proceeds through a fully coherent pathway, favoring the exceedingly fast propagation of energy throughout the system.[38–40]

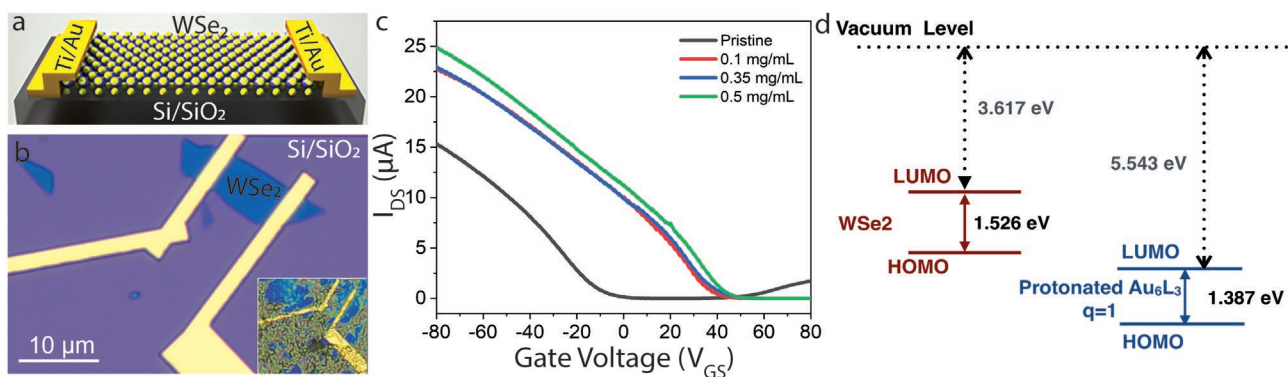GNCs are relatively stable in powder form or thin film under UV exposure. Notably, a small photobleaching has

Figure 5. a) The schematic diagram and b) optical microscope image of the back gated WSe$_2$ field effect transistor. Inset: optical micrograph of WSe$_2$ device after deposition of GNCs. c) Transfer plots (I_{DS}-V_{GS}) obtained from the multilayer WSe$_2$ device before and after deposition of different concentration of GNCs at V_{SD} = 0.5 V. d) Theoretical calculations for the HOMO-LUMO states of [Au(I)$_6$(TRZ)$_3$]$^+$ and multilayer WSe$_2$.

been observed during continuous UV exposure up to 14 h in our experiment (Figure S18, Supporting Information). Such extremely high photostability of the NCs is probably associated with the strong metal-ligand bonding and the compact structure of the ligand. In addition, the Au(I) states in these ultrasmall NCs could highly influence a strong LMCT transition characterized by high QY and excellent photostability. Furthermore, the NCs are highly stable at high temperature up to 150 °C and emit brilliant green-yellowish light even after treating at 100 °C for 1 h (Figure S19, Supporting Information).

2.4. GNCs as Dopants in Field-Effect Transistors

We fabricated a back-gated multilayer WSe$_2$ device, schematically represented in **Figure 5**a. The multilayer WSe$_2$ device (Figure 5b) has been characterized by measuring the drain-source current (I_{DS}) while sweeping the gate-source voltage (V_{GS}) in the range of ±80 V at a fixed drain-source voltage (V_{DS}) of 0.5 V at room temperature. The WSe$_2$ channel is ≈8 nm in thick, indicating 11–12 layers (Figure S20, Supporting Information).[41] The device depicts a *p*-dominant characteristic with relatively small electron current along positive V_{GS} (Figure 5c), suggesting that the Fermi level is inclined towards the valence band edge of WSe$_2$. With the further application of positive (negative) V_{GS}, the Fermi level is pushed towards the conduction band (valence band), respectively, thus injecting electrons (holes) in WSe$_2$. Interestingly, we found that the deposition of GNCs over WSe$_2$ significantly enhances the hole-current in this device, while electron-current is suppressed. Moreover, the threshold voltage (= V_{GS}), which is needed to turn on the device and extracted from the intercept of I_{DS}-V_{GS} plot, is shifted towards positive V_{GS}. More specifically, with 0.1 mg mL^{-1} solution of GNC-1 in DCM, threshold voltage has significantly shifted from −5 V to +42 V. The result suggests that WSe$_2$ device contains more positively charged carriers after deposition of GNCs, i.e., a non-degenerate *p*-doping is realized in WSe$_2$ in contact with the GNCs. With increasing the concentration of GNCs up to a certain extent, the I_{DS} continuously increases, and the threshold voltage shifts towards more positive V_{GS} values. This is due to the close proximity (0.4 eV) in between

the valence band (HOMO) of WSe$_2$ and the LUMO state of the protonated [Au(I)$_6$(TRZ)$_3$]$^+$ (Figure 5d), which allows the former as a donor and the GNCs as an acceptor.

3. Conclusion

We report for the first time atomically precise ultrasmall gold nanoclusters where all atoms are in the same valence state Au(I) and where they are sterically locked by specific dual ligand thiolate interactions to suppress vibrations to allow multifunctional electro-optical and quantum coherent behaviors. In particular, we report Au(I)$_6$ nanoclusters with steric locking of each atom by 6-(dibutylamino)-1,3,5-triazine-2,4-dithiol ligands, where a two-step chemical reaction was required to allow centrosymmetric octahedral structure. The underlying films produce a very strong THG response, very close to the high magnitude of the 2D monolayer metal dichalcogenide nanosheets, never observed before for gold nanoclusters. They also produce brilliant single and multiphoton luminescence response with exceptional stability. DFT calculations and femtosecond transient absorption studies suggest an ultrafast ligand-to-metal charge transfer with ultra-efficient intersystem crossing and demonstrate the role of quantum coherent effects in the photocycle. The quantum coherent behavior and relatively long decoherence time (200–300 fs) of the photoexcited GNCs allow extremely fast propagation of excitation from the core to the surrounding solvent. Finally, the Au(I) cores display marked electron-accepting properties also in the ground state, as we show in a proof-of-principle application as a *p*-dopant in 2D FET devices. In summary, these ultrasmall GNCs with interlocked 6 Au(I) atoms provide key insight for future applications as ultrafast photoswitches, or in emerging technologies such as quantum computing, since decoherence sets the maximum timeframe for the fully quantum operation of a device.

Supporting Information

Supporting Information is available from the Wiley Online Library or from the author.

Conflict of Interest

The authors declare no conflict of interest.

Data Availability Statement

The data that support the findings of this study are available from the corresponding author upon reasonable request.

[1] M. Zhou, C. Zeng, Q. Li, T. Higaki, R. Jin, *Nanomaterials* **2019**, *9*, 933.

[2] W. D. Si, Y. Z. Li, S. S. Zhang, S. Wang, L. Feng, Z. Y. Gao, C. H. Tung, D. Sun, *ACS Nano* **2021**, *15*, 16019.

[3] R. Jin, C. Zeng, M. Zhou, Y. Chen, *Chem. Rev.* **2016**, *116*, 10346.

[4] S. Chandra, Nonappa, G. Beaune, A. Som, S. Zhou, J. Lahtinen, H. Jiang, J. V. I. Timonen, O. Ikkala, R. H. A. Ras, *Adv. Opt. Mater.* **2019**, *7*, 1900620.

[5] V. Hynninen, S. Chandra, S. Das, M. Amini, Y. Dai, S. Lepikko, P. Mohammadi, S. Hietala, R. H. A. Ras, Z. Sun, O. Ikkala, Nonappa, *Small* **2021**, *17*, 2005205.

[6] I. Chakraborty, T. Pradeep, *Chem. Rev.* **2017**, *117*, 8208.

[7] S. Chandra, A. Sciortino, S. Shandilya, L. Fang, X. Chen, Nonappa, H. Jiang, L.-S. Johansson, M. Cannas, J. Ruokolainen, R. H. A. Ras, F. Messina, B. Peng, O. Ikkala, *Adv. Opt. Mater.* **2023**, *11*, 2201901.

[8] M. Zhu, C. M. Aikens, F. J. Hollander, G. C. Schatz, R. Jin, *J. Am. Chem. Soc.* **2008**, *130*, 5883.

[9] S. A. Miller, J. M. Womick, J. F. Parker, R. W. Murray, A. M. Moran, *J. Phys. Chem. C* **2009**, *113*, 9440.

[10] Z. Wu, R. Jin, *Nano Lett.* **2010**, *10*, 2568.

[11] M. S. Devadas, J. Kim, E. Sinn, D. Lee, T. Goodson, G. Ramakrishna, *J. Phys. Chem. C* **2010**, *114*, 22417.

[12] M. Zhou, C. Zeng, M. Y. Sfeir, M. Cotlet, K. Iida, K. Nobusada, R. Jin, *J. Phys. Chem. Lett.* **2017**, *8*, 4023.

[13] M. Y. Sfeir, H. Qian, K. Nobusada, R. Jin, *J. Phys. Chem. C* **2011**, *115*, 6200.

[14] T. D. Green, C. Yi, C. Zeng, R. Jin, S. Mcgill, K. L. Knappenberger, *J. Phys. Chem. A* **2014**, *118*, 10611.

[15] X. Kang, S. Wang, Y. Song, S. Jin, G. Sun, H. Yu, M. Zhu, *Angew. Chem., Int. Ed.* **2016**, *55*, 3611.

[16] K. L. D. M. Weerawardene, C. M. Aikens, *J. Am. Chem. Soc.* **2016**, *138*, 11202.

[17] K. L. D. M. Weerawardene, P. Pandeya, M. Zhou, Y. Chen, R. Jin, C. M. Aikens, *J. Am. Chem. Soc.* **2019**, *141*, 18715.

[18] Y. Song, J. Zhong, S. Yang, S. Wang, T. Cao, J. Zhang, P. Li, D. Hu, Y. Pei, M. Zhu, *Nanoscale* **2014**, *6*, 13977.

[19] S. S. Zhang, L. Feng, R. D. Senanayake, C. M. Aikens, X. P. Wang, Q. Q. Zhao, C. H. Tung, D. Sun, *Chem. Sci.* **2018**, *9*, 1251.

[20] N. Vermeulen, D. Castelló-Lurbe, M. Khoder, I. Pasternak, A. Krajewska, T. Ciuk, W. Strupinski, J. L. Cheng, H. Thienpont, J. Van Erps, *Nat. Commun.* **2018**, *9*, 2675.

[21] A. Taghizadeh, K. S. Thygesen, T. G. Pedersen, *ACS Nano* **2021**, *15*, 7155.

[22] A. Krasnok, M. Tymchenko, A. Alù, *Mater. Today* **2018**, *21*, 8.

[23] D. Nikogosyan, *Nonlinear Optical Crystals: A Complete Survey*, Springer, New York **2005**.

[24] G. Soavi, G. Wang, H. Rostami, D. G. Purdie, D. De Fazio, T. Ma, B. Luo, J. Wang, A. K. Ott, D. Yoon, S. A. Bourelle, J. E. Muench, I. Goykhman, S. Dal Conte, M. Celebrano, A. Tomadin, M. Polini, G. Cerullo, A. C. Ferrari, *Nat. Nanotechnol.* **2018**, *13*, 583.

[25] A. Autere, H. Jussila, Y. Dai, Y. Wang, H. Lipsanen, Z. Sun, *Adv. Mater.* **2018**, *30*, 1705963.

[26] Y. Cheng, H. Hong, H. Zhao, C. Wu, Y. Pan, C. Liu, Y. Zuo, Z. Zhang, J. Xie, J. Wang, D. Yu, Y. Ye, S. Meng, K. Liu, *Nano Lett.* **2020**, *20*, 8053.

[27] Z. Yu, B. Musnier, K. D. Wegner, M. Henry, B. Chovelon, A. Desroches-Castan, A. Fertin, U. Resch-Genger, S. Bailly, J. L. Coll, Y. Usson, V. Josserand, X. L. Guével, *ACS Nano* **2020**, *14*, 4973.

[28] L. Xiao, F. Wei, Y. Zhou, G. J. Anderson, D. M. Frazer, Y. C. Lim, T. Liu, Y. Xiao, *Nano Lett.* **2020**, *20*, 478.

[29] M. Lippitz, M. A. Van Dijk, M. Orrit, *Nano Lett.* **2005**, *5*, 799.

[30] R. Barbosa-Silva, M. L. Silva-Neto, D. Bain, L. Modesto-Costa, T. Andrade-Filho, V. Manzoni, A. Patra, C. B. De Araújo, *J. Phys. Chem. C* **2020**, *124*, 15440.

[31] J. Enkovaara, C. Rostgaard, J. J. Mortensen, J. Chen, M. Dułak, L. Ferrighi, J. Gavnholt, C. Glinsvad, V. Haikola, H. A. Hansen, H. H. Kristoffersen, M. Kuisma, A. H. Larsen, L. Lehtovaara, M. Ljungberg, O. Lopez-Acevedo, P. G. Moses, J. Ojanen, T. Olsen, V. Petzold, N. A. Romero, J. Stausholm-Møller, M. Strange, G. A. Tritsaris, M. Vanin, M. Walter, B. Hammer, H. Häkkinen, G. K. H. Madsen, R. M. Nieminen, et al., *J Phys Condens. Matter* **2010**, *22*, 253202.

[32] M. Kuisma, A. Sakko, T. P. Rossi, A. H. Larsen, J. Enkovaara, L. Lehtovaara, T. T. Rantala, *Phys. Rev. B Condens. Matter Mater. Phys.* **2015**, *91*, 115431.

[33] E. Makkonen, T. P. Rossi, A. H. Larsen, O. Lopez-Acevedo, P. Rinke, M. Kuisma, X. Chen, *J. Chem. Phys.* **2021**, *154*, 114102.

[34] T. P. Rossi, M. Kuisma, M. J. Puska, R. M. Nieminen, P. Erhart, *J. Chem. Theory Comput.* **2017**, *13*, 4779.

[35] L. Du, Y. Zhao, L. Wu, X. Hu, L. Yao, Y. Wang, X. Bai, Y. Dai, J. Qiao, M. G. Uddin, X. Li, J. Lahtinen, X. Bai, G. Zhang, W. Ji, Z. Sun, *Nat. Commun.* **2021**, *12*, 4822.

[36] C. Ruckebusch, M. Sliwa, P. Pernot, A. de Juan, R. Tauler, *J. Photochem. Photobiol. C: Photochem. Rev.* **2012**, *13*, 1.

[37] A. Sciortino, F. Ferrante, N. Mauro, G. Buscarino, L. Sciortino, G. Giammona, M. Cannas, D. Duca, F. Messina, *Carbon* **2021**, *173*, 454.

[38] R. Monni, G. Capano, G. Auböck, H. B. Gray, A. Vlček, I. Tavernelli, M. Chergui, *Proc. Natl. Acad. Sci. USA* **2018**, *115*, E6396.

[39] S. Rafiq, G. D. Scholes, *J. Phys. Chem. A* **2016**, *120*, 6792.

[40] Q. Bian, F. Ma, S. Chen, Q. Wei, X. Su, I. A. Buyanova, W. M. Chen, C. S. Ponseca, M. Linares, K. J. Karki, A. Yartsev, O. Inganäs, *Nat. Commun.* **2020**, *11*, 617.

[41] P. R. Pudasaini, A. Oyedele, C. Zhang, M. G. Stanford, N. Cross, A. T. Wong, A. N. Hoffman, K. Xiao, G. Duscher, D. G. Mandrus, T. Z. Ward, P. D. Rack, *Nano Res.* **2018**, *11*, 722.